Journal of Hazardous Materials 480 (2024) 136105

Contents lists available at ScienceDirect

Journal of Hazardous Materials

journal homepage: www.elsevier.com/locate/jhazmat

Coupled iron and heavy metal accumulation in karst soils in Southwestern China: Iron isotope perspective

Meng Qi [a,b], Chengshuai Liu [a,c], Ting Gao [a,*], Zhengrong Wang [d,e], Kadi Song [f], Yuhui Liu [a], Yafei Xia [a]

[a] State Key Laboratory of Environmental Geochemistry, Institute of Geochemistry, Chinese Academy of Sciences, Guiyang 550081, PR China
[b] University of Chinese Academy of Sciences, Beijing 100049, PR China
[c] College of Natural Resources and Environment, South China Agricultural University, Guangzhou 510642, PR China
[d] Department of Earth & Atmospheric Sciences, The City College of New York, CUNY, New York 10031, USA
[e] Graduate Center, CUNY, New York, NY 10016, USA
[f] Northwest University, College of Urban and Environmental Sciences, Xi'an 710127, PR China

HIGHLIGHTS

- Iron oxide formation controls Fe isotope fractionation in the saprolite layer.
- Litter input influences Fe isotope compositions in the soil layer.
- The behavior of Fe is linked to heavy metal accumulation in karst soils.

GRAPHICAL ABSTRACT

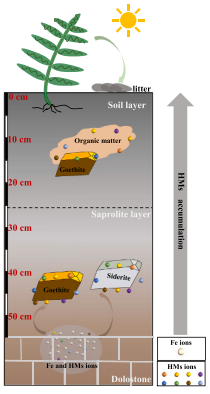

ARTICLE INFO

Keywords:
High geological background
Heavy metal
Fe isotopes
Karst soil
Mössbauer spectrum

ABSTRACT

Heavy metals (HMs) are abundant in the karst soils of Southwest China, posing significant health risks to millions of people. Iron (Fe) (hyr)oxides serve as critical carriers of HMs in these soils; however, the processes governing Fe oxide formation and transformation associated with HM accumulation during carbonate weathering in karst region is less understood. In this study, we present Fe isotope compositions from a carbonate–derived profile to investigate the major factors controlling Fe migration. In the saprolite layer, strong correlations between $\delta^{56}Fe_{bulk}$ and the proportions of extracted $Fe_{NH2OH.HCl}$ or $Fe_{residue}$ fractions suggest that the formation of goethite and phyllosilicate may be responsible for variations in $\delta^{56}Fe_{bulk}$. The positive correlations between $\delta^{56}Fe_{NH2OH.HCl}$ values and HM concentrations in this layer suggest an enhanced capacity for HM fixation by goethite in these soils. In contrast, the fractionation of Fe isotopes in the soil layer appears to be influenced by vegetation, as indicated by the correlation between total organic carbon and $\delta^{56}Fe_{bulk}$. The negative correlations between

* Corresponding author.
E-mail address: gaoting@mail.gyig.ac.cn (T. Gao).

https://doi.org/10.1016/j.jhazmat.2024.136105
Received 14 August 2024; Received in revised form 25 September 2024; Accepted 7 October 2024
Available online 9 October 2024

$\delta^{56}Fe_{bulk}$ values and HM concentrations in the soil layer likely indicate that vegetation litter enhances the retention capacity of Fe oxides for HMs. This study highlights the trajectory of Fe and its connection to HM accumulation in karst soil with high geological background levels.

1. Introduction

The soil in the karst region of Southwest China with abundant heavy metals (HMs) and a rich geological background has hindered the development of agricultural productivity [1]. Iron (Fe) and its oxides are important HM carriers in the soil and are involved in various processes such as the adsorption of arsenic (As) or zinc (Zn) [2,3], coprecipitation with cadmium (Cd) and chromium (Cr) [4,5], and immobilization of copper (Cu) and lead (Pb) by complexation with organic matter [6]. Therefore, improving our understanding of the behavior of Fe in karst soils is necessary.

Stable Fe isotopes are commonly used to fingerprint the behavior of Fe in soil [7,8]. Iron isotope fractionation in soil can reveal Fe migration in pedogenic processes such as the dissolution of primary minerals, formation of secondary minerals, redox reactions of Fe-bearing phases, and complexation with organic matter [9-13]. Isotopically light Fe (^{54}Fe) is preferentially eliminated into solution via proton-promoted dissolution of primary minerals (e.g., biotite) [14]. Liu et al. [15] reported that ^{54}Fe is preferentially released into aqueous solutions during chemical weathering, as demonstrated by river water analyses [10,16]. The Fe released from primary minerals precipitates as iron oxides (hematite and goethite) in soil under various conditions, which can be identified via Fe isotope fractionation. Qi et al. [17] reported that the zig–zag Fe isotope variation in a laterite profile was probably caused by the transformation of ferrihydrite to hematite and goethite. A fluctuating water table can induce distinct Fe isotope fractionation (−0.30 ‰ to 0.29 ‰) through the dissolution and/or precipitation of Fe-containing minerals such as goethite, demonstrating the redox processes in soil [13]. According to [10], the presence of the ^{54}Fe-rich signal in organic-rich soil indicated that Fe recycling is controlled by vegetation.

The behavior of Fe in soil was investigated using Fe isotopes in acidic or neutral soil. Studies revealed that it was primarily controlled by precipitation, reductive or proton-promoted dissolution, and complexation with organic matter [18,11,12,15,7,19]. The behavior of Fe in karst soil, with its alkaline environment (soil pH ≈ 8), likely differs from that in acidic or neutral silicate-derived soils, as the higher pH makes the mobilization of released Fe ions more difficult due to hydrolysis. For example, the hydrolysis of Fe^{3+} increased by 600-fold between pH 7.7 and 9.0 [20]. In this case, the free Fe ions in karst soil probably transform into goethite, as predicted by theoretical calculations from Combes et al. [21]. This transformation can further enhance the stability of Fe oxide-organic matter complexes in an alkaline environment. Nierop et al. [22] proposed that an increase in pH increases the dissociated and deprotonated acidic functional groups within organic matter, facilitating metal binding more readily than protonated groups at lower pH values. These differences in Fe behavior in alkaline and acidic soil might result in a distinct trajectory of Fe in karst soil compared to silicate-derived soil, such as laterite (pH ≈ 5) [17], promoting HM accumulation. Chemical extraction and big data analysis have revealed that Fe is crucial for HM accumulation in karst soil ([23]; Yang et al., 2021). However, few studies have focused on the influence of geochemical processes such as primary mineral dissolution, secondary mineral formation, and vegetation effects on Fe mobility and its association with HM accumulation in karst soil during carbonate weathering.

In this study, the mineralogy, major elements, and Fe isotope compositions of an in situ dolostone weathering profile from Guangxi, Southwestern China were systematically investigated. The focus was to (i) investigate the control of primary mineral dissolution, secondary mineral formation, and vegetation effects on Fe mobility, and (ii) reveal the relationship between Fe behavior and HMs to better understand HM accumulation in karst soils with high geological background levels.

2. Study area description and sample collection

The study site is the Huanjiang Observation and Research Station for karst ecosystems, which is operated by the Chinese Academy of Sciences. It is located in Huanjiang (HJ) County, situated in the northwestern Guangxi Zhuang Autonomous Region of Southwest China (115° 56′ 40″ E and 39° 42′ 36″ N) (Fig. 1a). This region is characterized by a subtropical, mountainous, and monsoon climate with a mean annual precipitation of ~1461 mm and a mean annual temperature of ~18.5 °C [24]. The rainy season spanning from April to August accounts for 60 % of the annual precipitation, whereas the dry period extends from September to March.

The HJ weathering profile developed on dolostone was collected from a small hill (Fig. 1b, elevation 461 m above sea level). Dolostone comprises 31 % calcium oxide (CaO) and 21 % magnesium oxide (MgO) [24]. The stratigraphic age of bedrock is Middle Carboniferous (~300 Ma) with the strata inclined at an angle of 278°∠10°. The surface soil layer (0–24 cm) is relatively fine grained, homogenous, and black (Munsell 5YR 3/2) with no signs of pedoturbation. Beneath the surface soil lies the saprolite layer (24–50 cm) comprising partially weathered brown dolostone (Munsell 5YR 5/10). Twenty-five samples were collected at ~2 cm intervals toward the bottom of the profile up to a total thickness of ~50 cm during July 2022. The soil was classified as dolomitic soil according to the World Reference Base for Soil Resources [25]. Three least-weathered bedrock samples were collected from below but near the regolith profile. The vegetation cover is dense, predominantly comprising Aspleniaceae, *Vitex negundo*, *Ligustrum lucidum*, and *Pyracantha fortuneana*. The stems and leaves of the typical plant Aspleniaceae were sampled near the regolith profile. The element cycling in the HJ profile was comprehensively assessed by collecting six local river water samples (~20 L) from the Xiaohuan Jiang River at the end of the rainy season from locations in proximity to the study sites (~10 km, Fig. 1c).

Each regolith sample (~2 kg) was collected and thoroughly mixed in the laboratory and air dried. The dried regolith sample (~100 g) was pulverized into particles of approximately 200 mesh size for subsequent chemical analysis. The stems and leaves were carefully wiped with a tissue to remove potential regolith contamination before being rinsed with Milli-Q ultrapure water, then dried at 105 °C, cut, and homogenized. The water samples were gathered in polyethylene plastic bottles prewashed with 5 % nitric acid (HNO_3) before sample collection. All of the samples were passed through a 0.45-μm cellulose acetate filter and promptly acidified to pH ~2 using distilled nitric acid prior to the analysis of iron concentrations and isotopes. The filtered suspended matter preserved in a centrifuge tube was dried using a freeze dryer.

3. Methods

The total organic carbon (TOC) and mineral compositions were detected following the analytical methods reported by Gao et al. [26] and Xia et al. [27], with a brief description provided in Section 3.1. The measurements of Fe species via Mössbauer spectroscopy (Section 3.2), sequential extraction experiment (Section 3.3), and Fe purification procedures (Section 3.4) are outlined.

3.1. Analysis of TOC content, mineral compositions, and trace element concentrations

The total organic carbon (TOC) content was performed by a Vario

MACRO cube (Elementar Analysensysteme GmbH, Germany) at State Key Laboratory of Environmental Geochemistry, Institute of Geochemistry, Chinese Academy of Sciences (IGCAS). Approximately 35 mg of sample powder was weighed into a tin container and then analyzed by dry combustion. The relative standard deviations (RSDs) of the results are below 0.5 %.

The mineral phases were determined by X-ray diffraction (XRD, Bruker D2, Germany) at the IGCAS. Samples were placed in a silicon sample holder with a low background value. The anode target of instrument was cobalt (Co), with a scan range of 5–85° at a rate of 1.2°/min and a step size of 0.02°. Quantitative analysis of mineral composition was conducted by TOPAS V5 software (Bruker AXS, Germany). The information of mineral crystal structures were derived from the COD database. The Rietveld method was chosen during the fitting process, and the fourth-order function was used. The background-subtracted residual (rwp) values were all lower than 16 % to ensure good fitting quality.

The concentrations of trace element were measured by inductively coupled plasma–mass spectrometry (ICP–MS, NexION 300X, PerkinElmer, USA). Measurements were preceded by drying about 100 mL of each liquid and digesting approximately 40 mg of each solid powder in a ~ 3.5 mL mixture of HF-HCl-HNO_3 in a 1:1:3 vol ratio. The samples were then dried again and dissolved in ~ 3 % HNO_3 for analysis. The internal standard Rh (10 μg L^{-1}) was utilized to correct for instrument drift. The GSS-5a, GSS-5, and GSS-3 (Chinese National Standard soil reference samples) were used for quality control. The accuracy of trace element measurements was within ± 5 % of the certified values for these standards. Repeated measurements (n = 3) of GSS-5a, GSS-5, and GSS-3 yielded a relative standard deviation (RSD) less than 10 %.

3.2. Mössbauer spectroscopy

In this study, Mössbauer spectra (MBS) of the samples were recorded and processed to identify the different oxidation states of Fe species using a high-velocity resolution Mössbauer spectrometer (MS-65, Science Engineering & Education Co, USA) at approximately 12 K. This was facilitated by the SHI-850 cryogenic system from Janis Research Co., Inc. (Wilmington, MA) at the Institute of Geochemistry, Chinese Academy of Sciences (IGCAS).

A cobalt (^{57}Co) source embedded in a rhodium (Rh) matrix emitted gamma rays with an energy of approximately 14.4 eV. Each sample, weighing between 20 and 40 mg, was loaded onto a copper sample holder featuring a window with a diameter of 1.0 cm and a thickness of around 0.3 cm to accommodate larger-sized samples. The precise weight of each sample was calculated to ensure the ideal absorber thickness, thereby optimizing the signal-to-noise ratio [28]. The measurements were conducted within a velocity range of ± 12 mm s^{-1} to detect any hyperfine split patterns (sextets) arising from magnetically ordered iron-bearing phases. Velocity calibration was performed using a 7-μm α-Fe foil, and all center shifts and peak positions were determined based on this standard reference material. The fitting results for the sample at a depth of 16–18 cm are shown in Fig. S1. The fitting parameters were quadrupole splitting (QS), magnetic field strength (T), and isomer shift (IS). Data quality assessment relied on the statistical criterion χ^2.

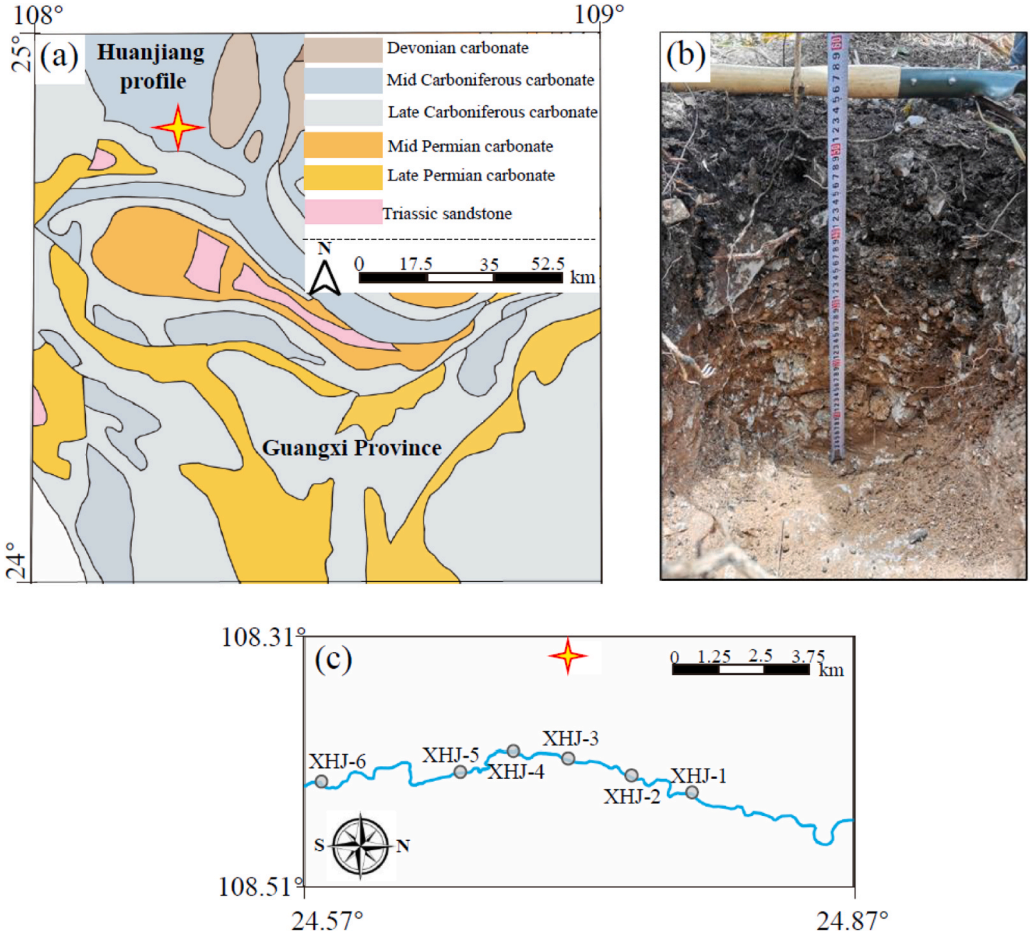

Fig. 1. Map showing the (a) geological setting, (b) dolostone weathering profile, and (c) localities of river water samples. The yellow stars represent sampling sites of the regolith profile.

3.3. Sequential extraction experiment

The sequential extraction method was employed to fractionate the three operationally defined Fe-bearing species from the selected samples [29,30]. The three Fe-bearing species are as mentioned: (a) siderite (a common Fe-bearing mineral in karst soils) soluble in ~5 % acetic acid (CH_3COOH, $Fe_{CH3COOH}$), (b) crystalline iron (oxyhydr)oxides soluble in ~1 mol L^{-1} hydroxylamine hydrochloride ($NH_2OH.HCl$, $Fe_{NH2OH.HCl}$), and (c) silicate-bound Fe ($Fe_{residue}$). The Fe concentration in the supernatant after each leaching step was determined via atomic absorption spectroscopy (PinAAcle900F, PE, USA) at IGCAS. The details of the sequential extraction procedure are provided in Supplementary Section.

3.4. Iron isotope measurements

The purification of Fe for isotopic analysis was conducted in laminar hoods of class-100 within a clean room of class-1000 at the IGCAS. The sample powder (~30 mg) was weighed into perfluoroalkane beakers (Savillex, USA). All of the samples were treated sequentially with ~2 mL of 3:1 (v/v) hydrogen fluoride (HF): nitric acid (HNO_3), ~2 mL of aqua regia, and ~6 mol L^{-1} hydrochloric acid (HCl). The last solution ensured the complete elimination of residual particulates for column chromatography.

The iron purification procedure described by He et al. [31] was followed. The Fe was chemically separated using approximately 1 mL of AG1X-8 resin in an HCl medium. The sequence of elution was calibrated via reference materials [Hawaiian Basalt (BHVO-2) and Guano Valley Andesite (AGV-2)] provided by the United States Geological Survey. The total procedural blank for Fe was small (<38 ng). The resin in the column was loaded with ~150 μg of Fe; thus, the blank had negligible influence on the samples.

The multicollector inductively coupled plasma mass spectrometer (Neptune Plus, Thermo Fisher, USA) was used to analyze Fe isotope ratio of each sample at IGCAS. Dilution to a concentration of about ~1 mg L^{-1} was performed on all samples and standards (IRMM-014 elemental Fe), utilizing a solution of ~3 % HNO_3. Utilizing the standard-sample bracketing method, the correction of the instrumental mass bias was carried out. To achieve reproducibility, a minimum of four iterations of the standard-sample sequence were performed for each sample. Eq. 1 was applied to report the Fe isotope ratios of the samples, which were expressed as deviations from the IRMM-014 standard.

$$\delta^{X}Fe = \left[\frac{\left({}^{X}Fe/{}^{54}Fe\right)_{sample}}{\left({}^{X}Fe/{}^{54}Fe\right)_{IRMM-014}} - 1\right] \times 1000 \quad (1)$$

where *x* refers to the mass of 56 or 57. The AGV-2 and BHVO-2 samples were analyzed, yielding average δ^{56}Fe values of 0.12 ± 0.02 ‰ and 0.13 ± 0.06 ‰, respectively, which are consistent with previously published data [32,31,33]. Replicate runs of BHVO-2 demonstrated a long-term external reproducibility for δ^{56}Fe of 0.04 ‰ (2 SD, n = 10) [17,34].

4. Results

4.1. Key physicochemical properties of soil and riverine samples

The pH and TOC of the HJ weathering profile are presented in Table 1. The pH values display a narrow range of 7.81–8.29. The TOC content is low in the saprolite layer (4.5–10.2 g kg^{-1}) but significant higher in the soil layer, with concentrations ranging from 20.4 to 83.8 g kg^{-1} (Fig. 2a). The specific conductance and oxidation—reduction potential of the river samples exhibit large variations from 242.2 μs cm^{-1} to 352.6 μs cm^{-1} and from −27.0 mV to −58.4 mV, respectively, while the pH of the river water shows limited variation from 7.17 to 7.63.

The average concentrations of nickel (Ni), Cu, Zn, As, Cd, Pb, antimony

Table 1
TOC, pH, mineral composition, and element concentration of soil in the HJ profile.

Depth	TOC	pH	chlorite	dolomite	illite	quartz	Fe_2O_3	TiO_2	Al_2O_3	La	Th	Sc	Ni	Zn	As	Cd	Pb	Sb	Cr	Cu
cm	g kg^{-1}		wt%							μg/g										
0 –2	75.1	7.81	26.7	16.2	40.2	16.9	6.80	0.74	15.36	61.90	15.10	16.20	104.00	341.00	77.30	7.93	60.80	4.67	158.00	16.40
4 –6	83.8	7.89	29.6	12.5	40.7	17.2	7.00	0.83	16.15	65.10	15.40	16.90	109.00	356.00	76.00	8.27	65.00	5.13	164.00	17.60
8 –10	72.6	7.91	22.4	24.1	37.2	16.3	7.00	0.82	16.03	67.00	15.80	17.50	112.00	354.00	79.50	8.27	62.20	4.89	168.00	17.30
12 –14	58.2	7.93	27.4	15.6	40.0	17.0	6.50	0.82	15.19	62.80	14.80	16.40	107.00	319.00	76.90	7.63	52.90	4.01	162.00	15.20
16 –18	42.5	7.97	21.1	33.1	30.9	14.8	5.80	0.63	13.16	54.20	12.80	14.50	95.20	268.00	76.60	6.57	41.00	2.70	144.00	12.40
20 –22	20.4	8.05	12.3	60.4	19.9	7.5	3.77	0.37	7.5	30.70	7.46	8.44	56.30	151.00	65.80	3.71	21.20	1.17	88.80	6.51
24 –26	10.2	8.17	0	83.0	12.6	4.5	2.21	0.18	4.69	18.90	4.74	5.23	35.90	92.90	60.10	2.41	12.50	0.64	58.10	3.99
28 –30	7.5	8.19	0	97.1	0	2.9	1.64	0.12	3.39	14.40	3.39	3.99	28.50	70.00	45.70	1.97	9.09	0.47	45.60	3.41
32 –34	7.2	8.19	0	93.2	0	6.9	2.62	0.24	5.31	21.50	5.37	6.03	40.70	108.00	48.40	2.57	14.00	0.56	61.90	4.26
36 –38	5.6	8.22	0	95.3	0	4.7	2.21	0.18	4.56	18.40	4.69	5.19	35.40	93.20	46.40	2.28	12.00	0.52	54.00	3.73
40 –42	4.8	8.22	0	95.4	0	4.6	2.11	0.21	4.38	17.50	4.47	4.89	33.60	89.10	47.10	2.12	11.20	0.46	50.80	3.62
44 –46	4.5	8.25	0	95.3	0	4.7	2.06	0.18	4.24	17.10	4.30	4.80	33.60	88.00	46.90	2.13	11.00	0.46	50.50	3.62
48 –50	5.3	8.29	0	92.3	0	7.7	2.76	0.26	5.69	23.30	5.83	6.54	43.70	119.00	49.40	2.63	14.90	0.56	64.40	4.51
Bedrock				100			0.02						4.38	3.60	41.60	0.57	0.24	0.03	8.10	0.57

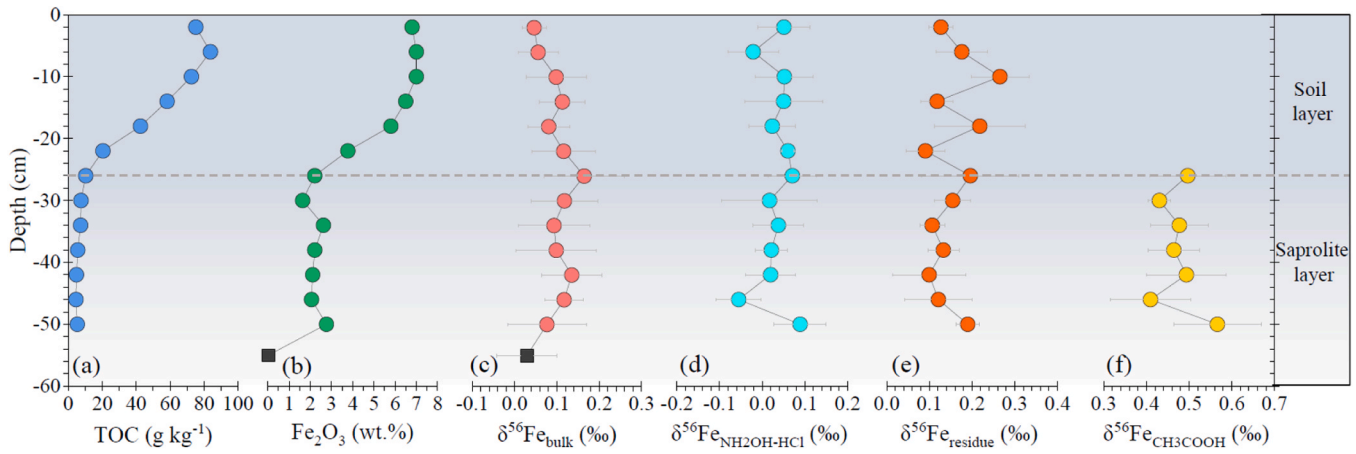

Fig. 2. Variations in (a) TOC, (b) Fe content, (c) $\delta^{56}Fe_{bulk}$, (d) $\delta^{56}Fe_{NH2OH.HCl}$, (e) $\delta^{56}Fe_{residue}$, and (f) $\delta^{56}Fe_{CH3COOH}$ with depth.

Table 2
Mössbauer spectroscopic measurements on bulk soil from the HJ profile.

Depth (cm)	Fe phases	IS (mm s^{-1})	STD	Magnetic field (T)	STD	QS (mm s^{-1})	STD	Line Width	STD	Proportion (%)	χ^2
0–2	Phyllosilicate(III)	0.39	0.01			0.45	0.03	0.58	0.05	62.42	1.24
	Goethite	0.25	0.03	36.67	1.38	0.04	0.06	0.58	0.11	37.58	
8–10	Phyllosilicate(III)	−0.04	0.02			0.37	0.03	0.58	0.04	41.54	1.22
	Goethite	−0.15	0.02	30.07	0.21	0.09	0.02	0.58	0.04	58.46	
16–18	Phyllosilicate(III)	−0.20	0.02			0.43	0.02	0.52	0.05	44.75	1.04
	Goethite	−0.36	0.02	35.06	0.12	0.13	0.04	0.58	0.06	55.25	
24–26	Phyllosilicate(III)	0.09	0.01			0.26	0.02	0.36	0.04	48.09	1.24
	Goethite	0.02	0.02	21.30	0.38	0.08	0.04	0.42	0.06	51.91	
32–34	Phyllosilicate(III)	0.55	0.04			0.49	0.03	0.58	0.07	44.00	1.21
	Goethite	0.49	0.05	40.64	0.12	0.20	0.05	0.58	0.07	56.00	
40–42	Phyllosilicate(III)	0.68	0.01			0.63	0.02	0.48	0.03	43.97	1.24
	Goethite	0.49	0.04	46.09	0.16	0.15	0.08	0.86	0.11	56.03	
48–50	Phyllosilicate(III)	−0.14	0.02			0.45	0.03	0.55	0.04	41.45	1.16
	Goethite	−0.25	0.01	35.30	0.05	0.14	0.03	0.58	0.05	58.55	

(Sb), and Cr in the saprolite layer are 35.9, 3.9, 94.3, 49.1, 2.3, 12.1, 0.5, and 55.0 μg g^{-1}, respectively, and those in the soil layer are 97.3, 14.2, 298.2, 75.4, 7.1, 50.5, 3.8, and 147.5 μg g^{-1}, respectively (Table 1).

4.2. Distribution of Fe in various phases

The X-ray diffractogram of the HJ profile shows fluctuation in the intensity of mineral-specific peaks. In the bedrock, nearly all XRD-detectable mineral phases consist of dolomite (Table 1). The saprolite layer predominantly contains dolomite (83.0–97.6 wt%) and quartz (2.9–7.7 wt%). In contrast, the mineral compositions in the soil layer include chlorite (12.3–29.6 wt%), dolomite (12.5–60.4 wt%), quartz (7.5–17.2 wt%), and illite (19.6–40.7 wt%).

The MBS analysis shows that at 12 K, Fe in the bulk regolith is distributed between two primary coordination environments: (a) Fe(III) as a sextet in goethite and (b) a quadrupole doublet in phyllosilicates (Table 2). In the saprolite layer, the distribution of Fe atoms in goethite and phyllosilicate is 51.91–58.55 % and 41.45–48.09 %, respectively, while in the soil layer, these values are 37.58–61.53 % for goethite and 38.47–62.42 % for phyllosilicate, respectively.

4.3. Fe concentrations and isotope compositions of bulk soils, sequential fractions, and suspended particulates

The Fe_2O_3 content in the bedrock is approximately 0.02 wt% (Table 1; Fig. 2b). In the saprolite layer, Fe_2O_3 concentrations exhibits limited variation, ranging from 1.64 to 2.76 wt% (Table 1; Fig. 2b). In contrast, Fe_2O_3 content in the soil layer is significantly higher, ranging from 3.77 to 7.00 wt%, and increases with decreasing depth. Table 3 and Fig. 2 display the Fe isotope compositions of all samples. The $\delta^{56}Fe$ values in the saprolite layer (0.08–0.16 ‰) are slightly higher than those in the bedrock (0.03 ± 0.07 ‰) and increase with decreasing depth. In the soil layer, the average $\delta^{56}Fe$ (0.05–0.12 ‰) is 0.08 ± 0.05 ‰, higher than that of the bedrock, but it decreases with decreasing depth.

Table 3 shows the proportions of extracted Fe fractions from samples at different depths. In the saprolite layer, the proportions of $Fe_{CH3COOH}$ (a minor proportion), $Fe_{NH2OH.HCl}$, and $Fe_{residue}$ are 0.2–0.4 %, 49.6–60.1 %, and 39.6–50.2 %, respectively. $Fe_{CH3COOH}$ is absent in the soil layer, where $Fe_{NH2OH.HCl}$ (29.1–58.3 %) and $Fe_{residue}$ (41.6–70.9 %) are dominant. The $\delta^{56}Fe$ values of $Fe_{NH2OH.HCl}$ in both the soil and saprolite layers (−0.06 ‰ to 0.09 ‰) are slightly lower than those of the bulk regolith (Table 3; Fig. 2d). Conversely, the $\delta^{56}Fe$ values (0.09–0.27 ‰) of $Fe_{residue}$ are higher than those of the bulk soil (Fig. 2e). Notably, the $\delta^{56}Fe$ values of $Fe_{CH3COOH}$ (0.41–0.57 ‰) are an order of magnitude higher than those of bulk soil (Fig. 2f). The $\delta^{56}Fe$ values for the different extracted fractions were verified via a mass balance approach, calculated using Eq. 2.

$$\delta^{56}Fe_{cal} = f_{CH3COOH} \times \delta^{56}Fe_{CH3COOH} + f_{NH_2OH-HCl} \times \delta^{56}Fe_{NH_2OH-HCl} + f_{residue} \times \delta^{56}Fe_{residue} \quad (2)$$

Here, f represents the proportion of Fe in the respective fractions. Adapting the error bars for the calculated total Fe value was done using Eq. 3.

$$2SD_{cal} = \sqrt{\left(f_{CH3COOH}2SD_{CH3COOH}\right)^2 + \left(f_{NH_2OH-HCl}2SD_{NH_2OH-HCl}\right)^2 + \left(f_{residue}2SD_{residue}\right)^2} \quad (3)$$

The calculated results presented in Table 3 are consistent with the measured Fe isotope composition of bulk soils within analytical errors.

The suspended particulates in the river samples exhibit an average Fe concentration of approximately 33.23 μg L^{-1}, with a range of 12.7–52.7 μg L^{-1}, consistent with the published values of 13.71–2199.42 μg L^{-1} [35]. The δ^{56}Fe values of the suspended particulates range from −0.01 ‰ to 0.05 ‰ with a mean value of 0.02 ± 0.06 ‰ (Table 3).

5. Discussion

5.1. Provenance tracing of the regolith

The origin of karst soils in Southwestern China is not clear, with three hypotheses proposed: (a) autochthonous origin, where soil forms from the insoluble residues of carbonate rocks [36]; (b) allochthonous origin, where soil develops from external sources like adjacent materials and eolian dust [37,38]; and (c) hybrid model, which posits that both sources contribute to soil formation [39]. The HJ profile in our study, located on a hilltop at an elevation of 461 m, suggests limited input from adjacent uplands. Notably, the $\delta^{56}Fe_{bulk\ soil}$ values are higher than those of the bedrock, which is in contrast with soils influenced by isotopically light Fe from adjacent materials [39]. The average Cd content in the soil (4.5 μg g^{-1}) does not match with silicate materials, where the upper crust averages only 0.08 μg g^{-1} (n = 41, [40], indicating that eolian dust is not the primary source. Moreover, the La—Th—Sc diagram shows that regolith from the HJ profile does not overlap with eolian dust (loess from northern China), suggesting a limited contribution from this source, as the studied location is influenced by dry and cold northern air flow (Fig. S2). Alternatively, the regolith likely derives from insoluble dolostone. The mineralogical analysis reveals a genetic relationship between the regolith and the underlying dolostone (Table 1). XRD analysis of insoluble residues from the bedrock shows the presence of margarite and aluminum oxides, indicating that silicates in the regolith is probably derived from dolostone weathering (Fig. S3). Bulk soil and bedrock data reveal positive correlations among several metals: Al_2O_3–Fe_2O_3 ($R^2 = 0.99$, $P < 0.05$, $n = 25$), Ti–Fe ($R^2 = 0.99$, $P < 0.05$, $n = 28$), Nb–Ta ($R^2 = 0.99$, $P < 0.05$, $n = 28$), and Zr–Hf ($R^2 = 0.99$, $P < 0.05$, $n = 28$) (Fig. S4). This indicates that these minerals likely weathered together over geological time, consistent with patterns observed in other carbonate-based weathering profiles [41,42]. Thus, we conclude that the HJ profile originates from the underlying dolostone.

5.2. Fe isotope fractionation during dolostone weathering

The patterns of Fe isotope variations in bulk soil across both layers display significant differences (Fig. 2). The increase in $\delta^{56}Fe_{bulk\ soil}$ with the decreasing depth in the saprolite layer probably reflects the control of secondary mineral formation, while the decreasing $\delta^{56}Fe_{bulk\ soil}$ with the increasing depth in the soil layer may indicate the influence of vegetation. Following are detailed discussions.

5.2.1. Role of leaching in saprolite and soil layers

Dolomite leaching experiments show that the leachate is enriched in light Fe isotopes compared to the residues, with a $\Delta^{56}Fe_{dolomite\text{-}leachate}$ value of 0.19 ‰ (Table 3). This finding is consistent with the heavy Fe isotope enrichment observed in the regolith of both layers compared to the bedrock (Table 3; Fig. 2c). Additionally, our results indicate that δ^{56}Fe values of suspended particulate matter are lower than those of regolith, indicating that ^{54}Fe is preferentially released from the regolith (Table 3). Although less Fe is present in dolomite (0.02 wt%), its dissolution results in high δ^{56}Fe values in the soil, probably inducing a negative correlation between Fe–Al and δ^{56}Fe. In the saprolite layer, the δ^{56}Fe value is negatively correlated with the Fe–Al ratio ($R^2 = 0.65$, $P < 0.05$, $n = 7$), consistent with the dolomite leaching results (Fig. 3a). However, no such correlation is found in the soil layer, indicating that leaching effects may be confounded by other processes (Fig. 3b).

5.2.2. Control of secondary mineral formation in the saprolite layer

Apart from the leaching process, the Fe isotope composition of soil may also be controlled by the formation of secondary minerals. Extracting experiments show that Fe is primarily concentrated in $Fe_{N\text{-}H2OH.HCl}$ and $Fe_{residue}$ fractions, with a small amount in $Fe_{CH3COOH}$ (<0.4 %) in the saprolite layer. MBS results suggest that Fe is mainly distributed in goethite and phyllosilicate (Table 2), implying that goethite is predominantly leached in $Fe_{NH2OH.HCl}$ while phyllosilicate remains in $Fe_{residue}$. A statistically significant positive correlation exists between $Fe_{residue}$ and $\delta^{56}Fe_{bulk\ soil}$, while a negative correlation is observed between $Fe_{NH2OH.HCl}$ and $\delta^{56}Fe_{bulk\ soil}$ in the saprolite layer (Fig. 4a). This pattern indicates that iron (hydr)oxides are enriched in light Fe isotopes, whereas residual mineral phases are enriched in heavy Fe isotopes, which is consistent with sequential leaching results (Table 3). This is also supported by the MBS results, indicating that the Fe isotope compositions of bulk regolith are closely related to the distribution of Fe atoms in goethite and phyllosilicate (Fig. 4b).

More specifically, the average Fe isotope offset ($\Delta^{56}Fe_{residue\text{-}NH2OH.HCl}$) between $Fe_{residue}$ (phyllosilicate) and $Fe_{NH2OH.HCl}$ (goethite) is ~0.08 ± 0.06 ‰ (1σ) in the saprolite layer, which is lower than the reported values (0.25 ± 0.37 ‰) [17]. This discrepancy can be explained through two pathways (Fig. 5). Path I: goethite can precipitate from Fe ions released from dolomite via precursor iron oxides such as ferrihydrite. Assuming the δ^{56}Fe of ferrihydrite is similar to that of dolomite-leached Fe (−0.16 ± 0.08 ‰, 2 SD), the δ^{56}Fe of goethite in the soil would range from approximately −0.02 ‰ to 0.16 ‰ (with $\Delta^{56}Fe_{goethite\text{–}ferrihydrite}$ values between 0.14 ‰ and 0.32 ‰) [43,44], consistent with the measured δ^{56}Fe of $Fe_{NH2OH.HCl}$ in the saprolite layer (−0.06 ‰ to 0.09 ‰) (Table 3). Path II: Fe ions released from phyllosilicate into goethite induce limited Fe isotope fractionation between the two. The relatively small $\Delta^{56}Fe_{phyllosilicate\text{–}goethite}$ value observed in both paths is probably owing to the alkaline soil environment. For Path I, ferrihydrite can convert to both goethite and hematite in silicate-derived soils under acidic conditions (e.g., laterite). For example, Qi et al. [17] reported an Fe isotope fractionation of 0.25 ± 0.37 ‰ between phyllosilicate and goethite, alongside hematite formation during basalt weathering (soil pH = 4.9). They suggested that hematite is enriched in isotopically heavy Fe, while goethite is enriched in isotopically light Fe, with a $\Delta^{56}Fe_{hematite\text{-}goethite}$ of 0.99 ± 0.18 ‰ (1σ). In our case, the absence of hematite reduces the Fe isotope offset between goethite and phyllosilicate, likely due to the lack of hematite-goethite transformation. This absence can be attributed to the alkaline conditions buffered by dolomite dissolution (soil pH = 8.2), where goethite is the predominant Fe-oxide phase that precipitates instead of hematite [45]. For Path II, in silicate-derived soils with acidic environments, the Fe

Table 3
Fe isotope compositions of regolith, extracted fractions, and riverine SPM Fe.

Depth (cm)	$\delta^{56}Fe_{bulk}$ (‰)	2 SD	$\delta^{56}Fe_{NH2OH.HCl}$ (‰)	2 SD	$\delta^{56}Fe_{residul}$ (‰)	2 SD	$\delta^{56}Fe_{CH3COOH}$ (‰)	2 SD	SPM	$\delta^{56}Fe_{SPM}$ (‰)	2 SD	$Fe_{NH2OH.HCl}$ (%)[b]	$Fe_{residual}$ (%)[b]	$Fe_{CH3COOH}$ (%)[a]	Fe_{cal}	2 SD_{cal}
0–2	0.05	0.03	0.05	0.06	0.13	0.03			XHJ−1	−0.01	0.06	29.1	70.9	0.0	0.10	0.09
4–6	0.06	0.05	−0.02	0.06	0.18	0.06			XHJ−2	0.01	0.04	57.7	42.3	0.0	0.06	0.08
8–10	0.10	0.07	0.05	0.07	0.27	0.07			XHJ−3	0.02	0.05	58.3	41.7	0.0	0.14	0.11
12–14	0.11	0.05	0.05	0.09	0.12	0.04			XHJ−4	0.05	0.06	56.4	43.6	0.0	0.08	0.06
16–18	0.08	0.05	0.02	0.05	0.22	0.11			XHJ−5	0.03	0.07	54.9	45.1	0.0	0.11	0.10
20–22	0.12	0.08	0.06	0.01	0.09	0.05			XHJ−6	0.02	0.05	58.3	41.6	0.1	0.07	0.05
24–26	0.16	0.09	0.07	0.06	0.20	0.11	0.50	0.09				49.6	50.2	0.2	0.13	0.10
28–30	0.12	0.08	0.02	0.11	0.15	0.04	0.43	0.03				53.6	46.2	0.3	0.08	0.07
32–34	0.09	0.08	0.04	0.06	0.11	0.03	0.48	0.07				59.3	40.5	0.3	0.07	0.05
36–38	0.10	0.09	0.02	0.04	0.13	0.04	0.46	0.06				60.1	39.6	0.3	0.07	0.05
40–42	0.14	0.07	0.02	0.06	0.10	0.09	0.49	0.09				57.9	41.7	0.4	0.05	0.04
44–46	0.12	0.05	−0.06	0.05	0.12	0.08	0.41	0.09				58.2	41.4	0.4	0.02	0.06
48–50	0.08	0.09	0.09	0.06	0.19	0.03	0.57	0.10				58.8	41.0	0.3	0.13	0.09
Bedrock	0.03	0.07					−0.16	0.08								

Abbreviations: SPM = suspended particulate matter; XHJ = Xiaohuan Jiang River.
[a] Proportion of extracted Fe in regolith.
[b] Fe content in silicate residues was calculated by subtracting the sum of two extracted solutions from the total concentration.

isotope offsets between phyllosilicate and goethite range from −0.62 ‰ to −0.82 ‰ based on experimental results [43,44]. These values are significantly lower than those observed in the saprolite layer ($\Delta^{56}Fe_{phyllosilicate\text{-}goethite}$ ~0.11 ‰). A possible explanation for this discrepancy is that dissolution mechanisms differ at low and high pH. Previous studies have shown that silicate dissolution is primarily controlled by silicon detachment at high pH, whereas at low pH, it is governed by the detachment of non-silicon structure-forming oxides [46].

Although $Fe_{CH3COOH}$ contains a low Fe concentration (<0.4 %), the leached fraction using acetic acid from soils has $\delta^{56}Fe$ values ranging from 0.41 ‰ to 0.57 ‰, which are higher than the $\delta^{56}Fe$ value of $Fe_{CH3COOH}$ from dolomite (−0.16 ± 0.08 ‰, Table 3). This indicates that $Fe_{CH3COOH}$ in the saprolite layer formed via dissolution and reprecipitation processes (siderite) rather than being inherited from the basal dolostone. However, precipitating $Fe_{CH3COOH}$ is challenging, as it requires pore fluid $\delta^{56}Fe$ between 0.91 ‰ and 1.07 ‰, given the fractionation factor of 0.5 ‰ between Fe in siderite (assuming that Fe in $Fe_{CH3COOH}$ is siderite) and its aqueous solution [47]. One possibility is that a small amount of ferrihydrite, enriched in isotopically heavy Fe and exhibiting a fractionation factor of 0.9 ± 0.2 ‰ between ferrihydrite and $Fe(II)_{aq}$ [43]. The ferrihydrite exists in equilibrium with Fe(II) released from dolomite dissolution (~−0.16 ‰). Subsequently, the Fe $(II)(OH)_{x(aq)}$ released during dolomite dissolution oxidizes to ferrihydrite, coprecipitating with the existing ferrihydrite (enriched in isotopically heavy Fe) to form secondary minerals ($Fe_{CH3COOH}$) with a high $\delta^{56}Fe$ value. Alternatively, the high $\delta^{56}Fe$ values of $Fe_{CH3COOH}$ may stem from the conversion of siderite (assuming that the Fe in the $Fe_{CH3COOH}$ fraction originates from siderite). Previous studies have indicated that siderite can transform into poorly crystalline Fe oxides in soils [48]. This transformation process could result in heavier Fe isotope compositions in the $Fe_{CH3COOH}$ pool due to the dissolution and/or subsequent re-precipitation of Fe during the conversion.

5.2.3. *Influence of the vegetation in the soil layer*

The $\delta^{56}Fe$ values in the soil layer exhibits weak correlations with $Fe_{NH2OH.HCl}$ and $Fe_{residue}$ ($n = 6$, $p > 0.05$, Fig. 6a). This lack of correlation is also apparent between the fraction of Fe atoms in goethite or phyllosilicate and the $\delta^{56}Fe$ of bulk soil (Fig. 6b), suggesting that secondary mineral formation along does not account for the variation in $\delta^{56}Fe$ values in the soil layer. However, a statistically significant positive correlation can be noted between TOC and Fe_2O_3, indicating that organic matter/vegetation may influence the variations in Fe concentrations and isotope compositions in the soil layer (Fig. 7a).

The metal isotope compositions of soil, including Fe, Mg, Zn, and molybdenum (Mo) are suggested to be influenced by organic matter complexation and vegetation growth [10,49-51]. Dideriksen et al. [52] demonstrated that organic complexes, such as desferrioxamine B and ethylenediaminetetraacetic acid, preferentially bind isotopically heavy Fe. If this binding process were dominant, a positive correlation between TOC and $\delta^{56}Fe$ of bulk soil would be expected, which contrasts with our observed trend (Fig. 7a). Alternatively, dissolved metal—organic complexes can enhance the transport of metals with low insolubility in soil [53], potentially leading to the enrichment of light Fe isotopes in soil due to the loss of isotopically heavy Fe that forms bonds with organic matter. This scenario could theoretically decrease Fe content but increase organic matter content, which again contrasts with our observed positive trend (Fig. 7a). Therefore, the potential Fe isotope fractionation associated with organic complexes in this study appears negligible. A plausible explanation for the observed trend of increasing $\delta^{56}Fe$ and decreasing Fe_2O_3 and TOC with depth in the soil layer is the uptake of Fe by plant roots from deeper layers and the deposition of leaf litter at the surface. Plants, such as rice, preferentially take up ^{54}Fe from soil with $\delta^{56}Fe$ values ranging from −3 ‰ to 0.5 ‰ [54]. The organic matter from dead plants, characterized by low $\delta^{56}Fe$, is deposited as litter at the top of the soil layer. This biological pump probably contributes to the

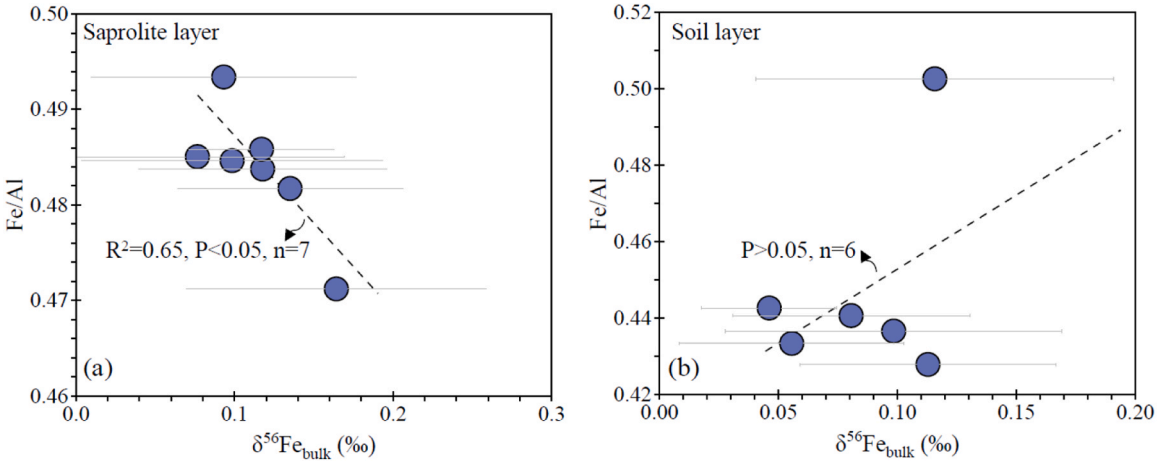

Fig. 3. Fe/Al ratio versus $\delta^{56}Fe_{bulk}$ in (a) saprolite and (b) soil layers. Al is used as an immobile element.

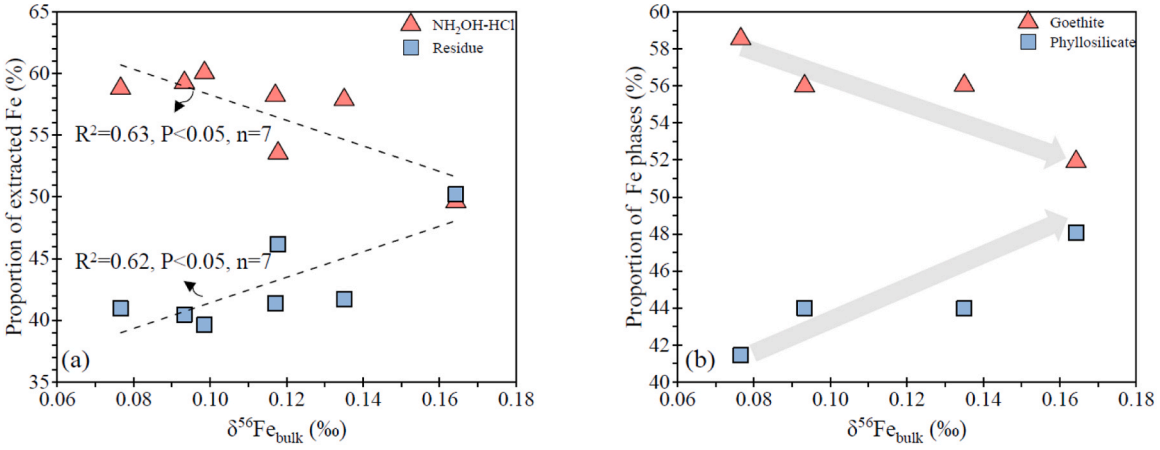

Fig. 4. $\delta^{56}Fe_{bulk}$ versus proportion of $Fe_{NH2OH.HCl}$ ($Fe_{residue}$) (a) and distribution of Fe atoms in goethite (phyllosilicate) (b) in the saprolite layer.

variation in δ^{56}Fe in bulk soil, in addition to processes such as dissolution and secondary mineral formation.

The quantitative assessment of the effects of vegetation litter on Fe isotope fractionation in the soil layer was conducted by designing a simple phenomenological model. Eq. 4, a linear equation, was formulated based on the observed trend of δ^{56}Fe increasing with depth in the saprolite layer.

$$\delta^{56}Fe_{bulk} = -0.002 * X + 0.1902 \quad (4)$$

Here, $\delta^{56}Fe_{bulk}$ is the δ^{56}Fe of bulk soil, and X is the depth in centimeters. When Fe isotope fractionation is not influenced by vegetation litter, the $\delta^{56}Fe$ of the surface soil (0–2 cm) should be approximately 0.186 ‰ (Fig. 7b). Consequently, the Fe isotope composition of vegetation litter in the topsoil (0–2 cm) is estimated to be −2.97 ‰ when the proportion of vegetation litter in the soil exceeds 4.3 %, allowing the δ^{56}Fe of the topsoil (0–2 cm) to reach 0.05 ‰.

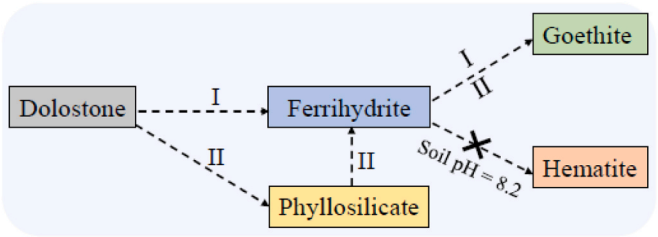

Fig. 5. Conceptual model of goethite formation in the saprolite layer. "I" and "II" refer to Path I and Path II, respectively, while "× " refers to limited hematite rather than its complete absence. Path I indicates that the source of Fe in goethite is from the dissolved dolomite, whereas Path II suggests that Fe in goethite is from phyllosilicate.

5.3. Implications of the HM accumulation in karst soils

The Q index is used to determine the degree of HM accumulation during the weathering process and is defined by Eq. 5 [55] as follows:

$$Qi = C_{i-soil}/C_{i-bedrock} \quad (5)$$

where C_i and $C_{i\text{-}bedrock}$ represent the element concentrations in soil and bedrock, respectively. The average Q_{Fe} values in saprolite and soil layers are 112 and 307, respectively. Similarly, the average Q_{HMs} (Ni, Cu, Zn, As, Cd, Pb, Sb, and Cr) in the saprolite layer are lower than those in the soil layer (Table S1), indicating that HM accumulation likely follows a similar pattern to that of Fe in the soil. This study indicates two stages of Fe accumulation during dolostone weathering: (i) the formation of Fe-bearing phases (goethite and phyllosilicate-Fe(III)) in the saprolite layer and (ii) the incorporation of Fe from vegetation inputs in the soil layer.

It is accepted that secondary minerals play a critical role in HM accumulation in karst soils [23,56,57]. However, HMs differ from Fe in that most HMs are challenging to mineralize in soil. Thus, HM

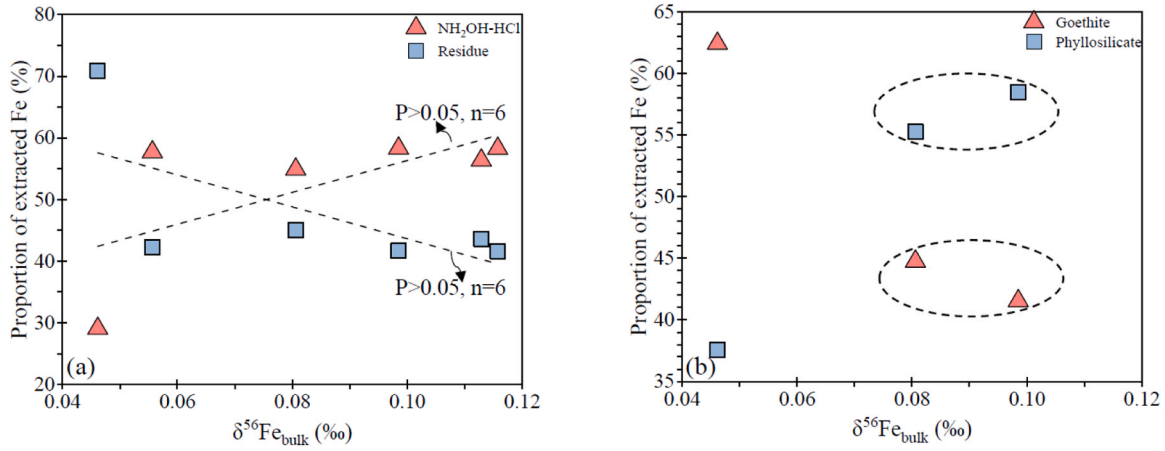

Fig. 6. $\delta^{56}Fe_{bulk}$ versus proportion of $Fe_{NH2OH.HCl}$ and $Fe_{residue}$ (a), and $\delta^{56}Fe_{bulk}$ versus distribution of Fe atoms in goethite and phyllosilicate (b) in the soil layer.

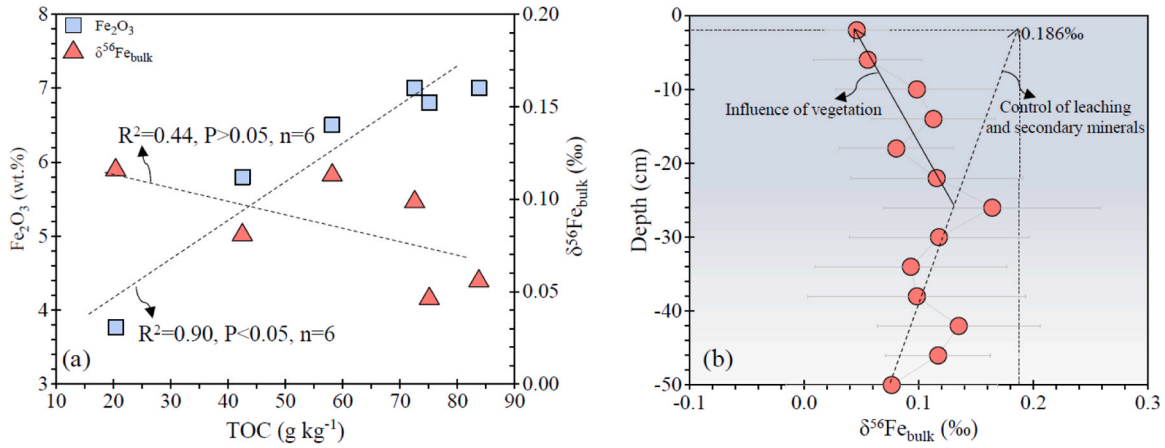

Fig. 7. TOC content versus Fe content and $\delta^{56}Fe_{bulk}$ (a), and the $\delta^{56}Fe_{bulk}$ values versus depth in the soil layer (b).

accumulation in the saprolite layer is probably controlled by the adsorption, coprecipitation, and substitution processes involving iron oxides. Indeed, Fe_2O_3 has a significant positive correlation with HM concentrations in the saprolite layer (Fig. 8a). Previous studies have also reported that the distributions of HMs (e.g., Cr, Zn, Cd, Pb) exhibit trends similar to those of Fe_2O_3 in soils undergoing carbonate weathering, which can be attributed to the adsorption mechanisms of Fe-oxide [58]. To further identify how Fe-bearing phases control the HM accumulation, the correlations between Fe isotope composition of extracted Fe pools and HM concentration were conducted in the saprolite layer. As shown in Fig. S5a, the correlations between $\delta^{56}Fe_{residue}$ and HM concentration are weak (e.g., Zn, Pb, Ni, Cr, Cd, $r < 0.34$), indicating that the mobilization of Fe preserved in phyllosilicate has a negligible influence on HM accumulation in this layer. In contrast, positive correlations were found between $\delta^{56}Fe_{NH2OH.HCl}$ values and HM concentration (Zn, Pb, Ni, Cr, Cd, As, Sb, Cu, $r > 0.53$, Fig. S5b). As discussed above,$\delta^{56}Fe_{NH2OH.HCl}$ values are controlled by Fe release from phyllosilicate and dolomite. With increasing weathering, the released Fe from these sources become heavier due to the preferential loss of isotopically light Fe, resulting in higher $\delta^{56}Fe_{NH2OH.HCl}$ values. Meanwhile, the crystallinity of Fe oxides—mainly composed by goethite, according to Mössbauer results—increases with weathering, enhancing HM fixation and contributing to higher HM concentrations. This observation aligns with findings by Yang et al. [59], who noted that the growth of ferromanganese nodules (mainly goethite) is associated with high HM concentration in karst soils. In addition, we found positive correlations between $\delta^{56}Fe_{CH3COOH}$ values and HM in the saprolite layer (Fig. S5c). Given that $\delta^{56}Fe_{CH3COOH}$ values are influenced by the transformation between siderite and ferrihydrite, these transformations may also contribute to HM accumulation in the saprolite layer, despite the limited proportion of the $Fe_{CH3COOH}$ fraction.

In contrast to the saprolite layer, the average Q_{HMs} (Ni, Cu, Zn, As, Cd, Pb, Sb, and Cr) values in the soil layer are higher. The individual process of secondary minerals does not fully interpret the sharp accumulation of HMs in the soil layer. The Fe accumulation in the soil layer suggests that HM accumulation is also probably influenced by the input of vegetation litter. Considering the TOC in the soil and the Ni, Zn, Cd, Pb, Sb, Cr, and Cu concentrations in the organic matter estimated from the average element concentration in bulk vegetation (Table S2), the contributions of these metals from vegetation litter to the soil are less than ~3 %. This indicates that vegetation litter has a small influence on HM accumulation in the soil layer. However, the high TOC of 58.8 g kg^{-1} in the soil likely facilitates the binding of HMs to iron oxides. Wan et al. [60] reported that organic matter can promote the binding of Pb to iron oxides in subtropical soils. The slopes of the Fe_2O_3-HMs relationships in the soil layer are greater than those in the saprolite layer: Ni: 16.5 vs. 13.4, Zn: 63.3 vs. 41.8, Cd: 1.4 vs. 0.6, Pb: 13.2 vs. 5.2, Sb: 1.2 vs. 0.1, Cr: 23.7 vs. 17.5, and Cu: 3.7 vs. 1.0. Thus, the ability of Fe to accumulate HMs is enhanced by the input of vegetation litter. This is supported by the positive correlations observed between TOC and HM concentrations (Fig. 8d). In addition, negative correlations between $\delta^{56}Fe_{bulk}$ values and HM concentrations were observed in the soil layer (Fig. S5d). As explained above, $\delta^{56}Fe_{bulk}$ values in this layer are likely influenced by the input of vegetation litter.

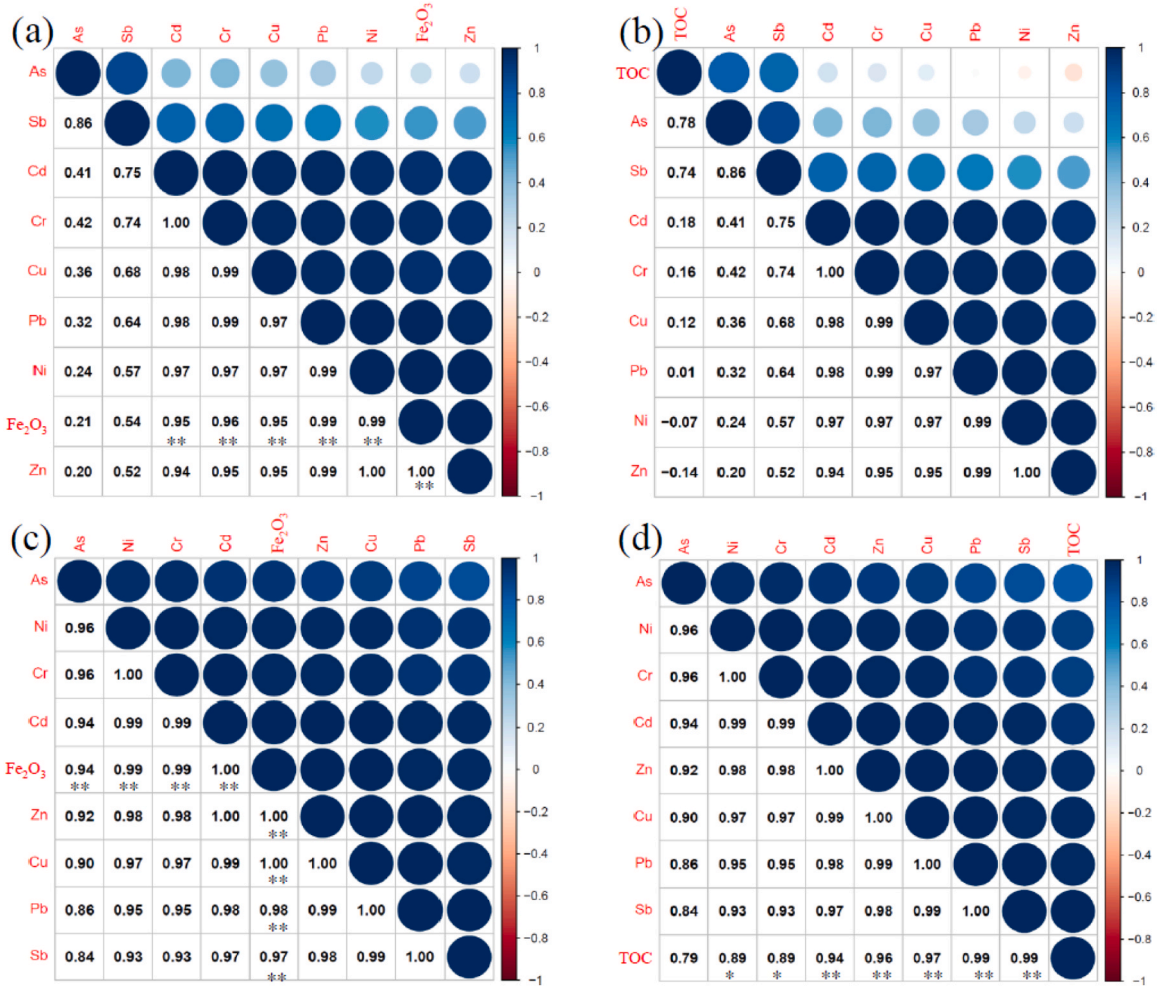

Fig. 8. Correlation matrix among HM concentration, Fe_2O_3 (a), and TOC content (b) in the saprolite layer. Correlation matrix among HM concentration, Fe_2O_3 (c), and TOC content (d) in the soil layer. * *: Significant at $p < 0.01$. * : Significant at $p < 0.05$.

Therefore, it can be inferred that the input of vegetation litter not only enhances the retention capacity of Fe oxides for HMs but also induces a significant negative shift in Fe isotope composition in the surface soils.

In summary, a conceptual model can be proposed based on the Fe isotope signals in soils, emphasizing the roles of Fe oxide formation and organic matter complexation in HM accumulation (Fig. 9). In the saprolite layer, the positive correlations between $\delta^{56}Fe_{NH2OH.HCl}$ or $\delta^{56}Fe_{CH3COOH}$ values and HM concentrations indicate that the aging of goethite and the transformation of siderite play an important role in HM accumulation. In the soil layer, the negative shift in $\delta^{56}Fe_{bulk\ soil}$ values likely reflects an increased capacity of Fe oxides to accumulate HM in the presence of vegetation litter. These findings suggest that the Fe isotope composition of bulk soil and its extracted fractions can provide new insights into HM accumulation driven by Fe behavior in soils. This offers a microscopic basis for controlling HM immobilization and release in Fe oxides in areas with high geological backgrounds.

6. Conclusions

This study revealed that the $\delta^{56}Fe$ values in bulk soil are higher than those of parent dolostone, indicating that ^{54}Fe enters the hydrosphere preferentially. In the saprolite layer, the Fe isotope composition is primarily controlled by the formation of phyllosilicate and goethite. The lighter Fe isotope signatures observed in the soil layer are attributed to the influence of organic matter, which is characterized by isotopically light Fe. According to the correlations between $\delta^{56}Fe$ values and HM concentrations in the saprolite layer, it is proposed that HM accumulation is associated with the crystallinity of goethite. In contrast, the accumulation of HMs in the soil layer is further enhanced by the input of vegetation litter, which amplifies the influence of Fe-(hyr)oxides. This study improves our comprehension of the connection between the formation and/or transformation of Fe-(hyr)oxides and HM accumulation in karst soils with high geological background.

Environmental implication

Heavy metals (HMs) are abundant in the karst soils of Southwest China, posing health risks to millions. Iron (Fe) (hydr)oxides are key carriers of HMs, but the processes driving their formation and transformation during HM accumulation in carbonate weathering remain poorly understood. In this study, we utilized stable Fe isotopes and Mössbauer spectroscopy to trace the trajectory of Fe and establish its connection with HM accumulation in soils during carbonate weathering. This research enhances our understanding of Fe dynamics and HM accumulation in regions with a high geological background.

CRediT authorship contribution statement

Yafei Xia: Data curation. **Chengshuai Liu:** Supervision, Resources, Funding acquisition. **Meng Qi:** Writing – original draft. **Zhengrong Wang:** Formal analysis. **Ting Gao:** Writing – review & editing, Supervision, Methodology, Conceptualization. **Yuhui Liu:** Data curation.

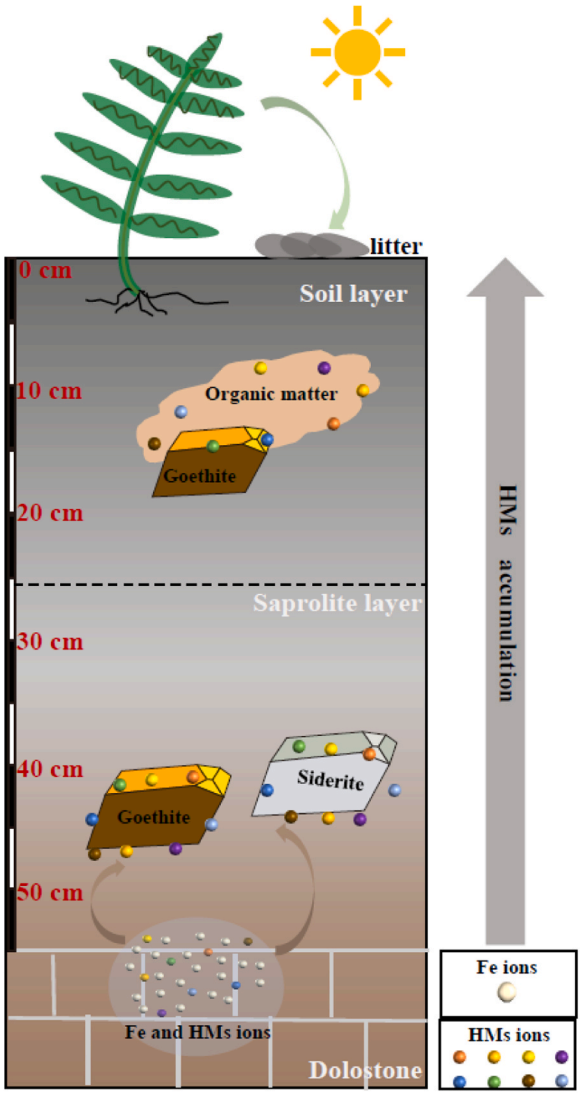

Fig. 9. Conceptual model of HM accumulation in saprolite and soil layers.

Kadi Song: Data curation.

Declaration of Competing Interest

The authors declare that they have no known competing financial interests or personal relationships that could have appeared to influence the work reported in this paper.

Acknowledgments

We would like to express our gratitude to Yang Tang for invaluable assistance in the MC-ICPMS laboratory. Additionally, we extend our appreciation to Fei Wu for their valuable support in analyzing Mössbauer spectroscopic data. This work was financially supported by the National Natural Science Foundations of China (42330712 and 42025705) and Guizhou Province High-level Talent Project (GCC [2022]002-1).

Appendix A. Supporting information

Supplementary data associated with this article can be found in the online version at doi:10.1016/j.jhazmat.2024.136105.

Data Availability

Data will be made available on request.

References

[1] Ma, X.D., Guan, D.X., Zhang, C.S., Yu, T., Li, C., Wu, Z.L., et al., 2024. Improved mapping of heavy metals in agricultural soils using machine learning augmented with spatial regionalization indices. J Hazard Mater 478, 135407.
[2] Liu, Y.H., Liu, C.S., Wu, F., Xia, Y.F., Qi, M., Gao, T., 2024. Zinc isotope fractionation during coprecipitation with amorphous iron (hydr)oxides. Geochim Cosmochim Acta 379, 158–171.
[3] Rawson, J., Siade, A., Sun, J., Neidhardt, H., Berg, M., Prommer, H., 2017. Quantifying reactive transport processes governing arsenic mobility after injection of reactive organic carbon into a Bengal Delta aquifer. Environ Sci Technol 51 (15), 8471–8480.
[4] Frierdich, A.J., Scherer, M.M., Bachman, J.E., Engelhard, M.H., Rapponotti, B.W., Catalano, J.G., 2012. Inhibition of trace element release during Fe(II)-activated recrystallization of Al-, Cr-, and Sn-substituted goethite and hematite. Environ Sci Technol 46 (18), 10031–10039.
[5] Liu, L., Wang, X.M., Zhu, M.Q., Ma, J.Y., Zhang, J., Tan, W.F., et al., 2019. The speciation of Cd in Cd-Fe co-precipitates: does Cd substitute for Fe in goethite structure? ACS Earth Space Chem 3 (10), 2225–2236.
[6] Martínez, C.E., McBride, M.B., 1999. Dissolved and labile concentrations of Cd, Cu, Pb, and Zn in aged ferrihydrite−organic matter systems. Environ Sci Technol 33 (5), 745–750.
[7] Poitrasson, F., Viers, J., Martin, F., Braun, J.J., 2008. Limited iron isotope variations in recent lateritic soils from Nsimi, Cameroon: Implications for the global Fe geochemical cycle. Chem Geol 253, 54–63.
[8] Yesavage, T., Stinchcomb, G.E., Fantle, M.S., Sal, P.B., Kasznel, A., Brantley, S.L., 2016. Investigation of a diabase-derived regolith profile from Pennsylvania: mineralogy, chemistry and Fe isotope fractionation. Geoderma 273, 83–97.
[9] Brantley, S.L., Liermann, L.J., Guynn, R.L., Anbar, A., Icopini, G.A., Barling, J., 2004. Fe isotopic fractionation during mineral dissolution with and without bacteria. Geochim Cosmochim Acta 68, 3189–3204.
[10] Fantle, M.S., DePaolo, D.J., 2004. Iron isotopic fractionation during continental weathering. Earth Planet Sci Lett 228, 547–562.
[11] Kiczka, M., Wiederhold, J.G., Frommer, J., Voegelin, A., Kraemer, S.M., Bourdon, B., et al., 2011. Iron speciation and isotope fractionation during silicate weathering and soil formation in an alpine glacier forefield chronosequence. Geochim Cosmochim Acta 75, 5559–5573.
[12] Li, M., He, Y.-S., Kang, J.-T., Yang, X.-Y., He, Z.-W., Yu, H.-M., et al., 2017. Why was iron lost without significant isotope fractionation during the lateritic process in tropical environments? Geoderma 290, 1–9.
[13] Mansfeldt, T., Schuth, S., Häusler, W., Wagner, F.E., Kaufhold, S., Overesch, M., 2012. Iron oxide mineralogy and stable iron isotope composition in a Gleysol with petrogleyic properties. J Soils Sediment 12, 97–114.
[14] Kiczka, M., Wiederhold, J.G., Frommer, J., Kraemer, S.M., Bourdon, B., Kretzschmar, R., 2010. Iron isotope fractionation during proton- and ligand-promoted dissolution of primary phyllosilicates. Geochim Cosmochim Acta 74, 3112–3128.
[15] Liu, S.A., Teng, F.Z., Li, S., Wei, G.J., Ma, J.L., Li, D., 2014. Copper and iron isotope fractionation during weathering and pedogenesis: insights from saprolite profiles. Geochim Cosmochim Acta 146, 59–75.
[16] Ingri, J., Conrad, S., Lidman, F., Nordblad, F., Engström, E., Rodushkin, I., et al., 2018. Iron isotope pathways in the boreal landscape: role of the riparian zone. Geochim Cosmochim Acta 239, 49–60.
[17] Qi, M., Gao, T., Wang, Z.R., Liu, Y.H., Xia, Y.F., Song, C.S., et al., 2022. Iron solid-phase differentiation controls isotopic fractionation during lateritic weathering of basalt. CATENA 217, 106512.
[18] Fekiacova, Z., Pichat, S., Cornu, S., Balesdent, J., 2013. Inferences from the vertical distribution of Fe isotopic compositions on pedogenetic processes in soils. Geoderma 209–210, 110–118.
[19] Thompson, A., Ruiz, J., Chadwick, O.A., Titus, M., Chorover, J., 2007. Rayleigh fractionation of iron isotopes during pedogenesis along a climate sequence of Hawaiian basalt. Chem Geol 238, 72–83.
[20] Sunda, W., Huntsman, S., 2003. Effect of pH, light, and temperature on Fe–EDTA chelation and Fe hydrolysis in seawater. Mar Chem 84, 35–47.
[21] Combes, J.M., Manceau, A., Calas, G., Bottero, J.Y., 1989. Formation of ferric oxides from aqueous solutions: a polyhedral approach by X-ray absorption spectroscdpy: I. Hydrolysis and formation of ferric gels. Geochim Cosmochim Acta 53 (3), 583–594.
[22] Nierop, K.G.J., Jansen, B., Verstraten, J.M., 2002. Dissolved organic matter, aluminium and iron interactions: precipitation induced by metal/carbon ratio, pH and competition. Sci Total Environ 300, 201–211.
[23] Wen, Y.B., Li, W., Yang, Z.F., Zhang, Q.Z., Ji, J.F., 2020. Enrichment and source identification of Cd and other heavy metals in soils with high geochemical background in the karst region, Southwestern China. Chemosphere 245, 125620.
[24] Wang, F., Zhang, J., Lian, J.J., Fu, Z., Y, Luo, Z.D., et al., 2022. Spatial variability of epikarst thickness and its controlling factors in a dolomite catchment. Geoderma 428, 116213.
[25] IUSS Working Group WRB, 2022. World Reference Base for Soil Resources. International soil classification system for naming soils and creating legends for soil maps, 4th ed. International Union of Soil Sciences (IUSS), Vienna, Austria.

[26] Gao, T., Qi, M., Wang, Z.R., Yin, R.S., Liu, C.S., Liu, Y.H., et al., 2023. Magnesium isotope variations in granite regoliths from two contrasting climates. J Geophys Res Earth Surf. https://doi.org/10.1029/2023JF007217.
[27] Xia, Y.F., Liu, Y.H., Liu, C.S., Gao, T., Yin, R.S., Qi, M., et al., 2023. Lake sediment archive reveals a distinct response to anthropogenic Pb and Zn deposition with historical periods: Pb–Zn isotope evidence. Environ Sci Technol 57 (40), 15184–15192.
[28] Kumar, A., Singh, M.R., Sarma, P.R., Tripathi, K.C., 1989. Optimised thickness of diffusive Mossbauer absorbers. J Phys D 22 (3), 465.
[29] Rego, E.S., Busigny, V., Philippot, P., 2022. Chemical extraction of iron from carbonate in banded iron formations for isotope analysis. Chem Geol 611, 121120.
[30] Wiederhold, J.G., Teutsch, N., Kraemer, S.M., Halliday, A.N., Kretzschmar, R., 2007. Iron isotope fractionation in oxic soils by mineral weathering and podzolization. Geochim Cosmochim Acta 71, 5821–5833.
[31] He, Y.S., Ke, S., Teng, F.Z., Wang, T., Wu, H., Lu, Y., et al., 2015. High-precision iron isotope analysis of geological reference materials by high-resolution MC-ICP-MS. Geostand Geoanal Res 39, 341–356.
[32] Craddock, P.R., Dauphas, N., 2010. Iron isotopic compositions of geological reference materials and chondrites. Geostand Geoanal Res 35, 101–123.
[33] Millet, M.-A., Baker, J.A., Payne, C.E., 2012. Ultra-precise stable Fe isotope measurements by high resolution multiple-collector inductively coupled plasma mass spectrometry with a ^{57}Fe-^{58}Fe double spike. Chem Geol 304–305, 18–25.
[34] Wu, Q.Q., Liu, C.S., Wang, Z.R., Gao, T., Liu, Y.H., Xia, Y.F., et al., 2022. Zinc regulation of iron uptake and translocation in rice (Oryza sativa L.): implication from stable iron isotopes and transporter genes. Environ Pollut, 118818.
[35] Song, L.T., Liu, C.-Q., Wang, Z.-L., Zhu, X.-K., Teng, Y.G., Liang, L.L., et al., 2011. Iron isotope fractionation during biogeochemical cycle: information from suspended particulate matter (SPM) in Aha Lake and its tributaries, Guizhou, China. Chem Geol 280, 170–179.
[36] Ji, H.B., Wang, S.J., Ouyang, Z.Y., Zhang, S., Sun, C.X., Liu, X.M., et al., 2004. Geochemistry of red residua underlying dolomites in karst terrains of Yunnan-Guizhou Plateau I. The formation of the Pingba profile. Chem Geol 203, 1–27.
[37] Jackson, M.L., 1982. Eolian influence on terra rossa soils of Italy traced buy quartz oxygen isotope ratio. Int Clay Conf.
[38] Muhs, D.R., Budahn, J.R., 2009. Geochemical evidence for African dust and volcanic ash inputs to terra rossa soils on carbonate reef terraces, northern Jamaica, West Indies. Quatern Int 196, 13–35.
[39] Feng, J.-L., Pei, L.-L., Zhu, X., Ju, J.-T., Gao, S.-P., 2018. Absolute accumulation and isotope fractionation of Si and Fe during dolomite weathering and terra rossa formation. Chem Geol 476, 340–351.
[40] Hu, Z.C., Gao, S., 2008. Upper crustal abundances of trace elements: a revision and update. Chem Geol 253, 205–221.
[41] Chen, M.Z., Li, X.X., Cao, X.X., Yang, W.T., Wu, P., Hao, H.Y., et al., 2024. Soil-forming accumulation of heavy metals in geological high background areas: constraints of structure, lithology, and overlying soil geochemistry. J Geochem Explor 263, 107518.
[42] Ji, H.B., Chang, C., Beckford, H.O., Song, C.S., Blake, R.E., 2021. New perspectives on lateritic weathering process over karst area-Geochemistry and Si-Li isotopic evidence. Catena 198, 105022.
[43] Bullen, T.D., White, A.F., Childs, C.W., Vivit, D.V., Schulz, M.S., 2001. Demonstration of significant abiotic iron isotope fractionation in nature. Geology 29, 699–702.
[44] Frierdich, A.J., Beard, B.L., Reddy, T.R., Scherer, M.M., Johnson, C.M., 2014. Iron isotope fractionation between aqueous Fe(II) and goethite revisited: new insights based on a multi-direction approach to equilibrium and isotopic exchange rate modification. Geochim Cosmochim Acta 139, 383–398.
[45] Jolivet, J.P., Chanéac, C., Tronc, E., 2004. Iron oxide chemistry. From molecular clusters to extended solid networks. Chem Comn (5).
[46] Brady, P., Walther, J.V., 1989. Controls on silicate dissolution rates in neutral and basic pH solutions at 25°C. Geochim Cosmochim Acta 53, 2823–2830.
[47] Wiesli, R.A., Beard, B.L., Johnson, C.M., 2004. Experimental determination of Fe isotope fractionation between aqueous Fe(II), siderite and "green rust" in abiotic systems. Chem Geol 211, 343–362.
[48] Sánchez-Alcalá, I., Bellón, F., del Campillo, M.C., Barrón, V., Torrent, J., 2012. Application of synthetic siderite ($FeCO_3$) to the soil is capable of alleviating iron chlorosis in olive trees. Sci Hortic 138, 17–23.
[49] Opfergelt, S., Cornelis, J.T., Houben, D., Givron, C., Burton, K.W., Mattielli, N., 2017. The influence of weathering and soil organic matter on Zn isotopes in soils. Chem Geol 466, 140–148.
[50] Ryu, J.-S., Vigier, N., Derry, L., Chadwick, O.-A., 2021. Variations of Mg isotope geochemistry in soils over a Hawaiian 4 Myr chronosequence. Geochim Et Cosmochim Acta 292, 94–114.
[51] Siebert, C., Pett-Ridge, J.C., Opfergelt, S., Guicharnaud, R.A., Halliday, A.N., Burton, K.W., 2015. Molybdenum isotope fractionation in soils: influence of redox conditions, organic matter, and atmospheric inputs. Geochim Cosmochim Acta 162, 1–24.
[52] Dideriksen, K., Baker, J.A., Stipp, S.L.S., 2008. Equilibrium Fe isotope fractionation between inorganic aqueous Fe(III) and the siderophore complex, Fe(III)-desferrioxamine B. Earth Planet Sci Lett 269, 280–290.
[53] Ma, J.-L., Wei, G.-J., Xu, Y.-G., Long, W.-G., Sun, W.-D., 2007. Mobilization and re-distribution of major and trace elements during extreme weathering of basalt in Hainan Island, South China. Geochim Cosmochim Acta 71, 3223–3237.
[54] Wu, B., Amelung, W., Xing, Y., Bol, R., Berns, A.E., 2019. Iron cycling and isotope fractionation in terrestrial ecosystems. Earth-Sci Rev 190, 323–335.
[55] Xie, D.X., Yang, Y., Su, C.T., Meng, X.J., 2015. Contrasts of geochemical characteristics and environmental quality between soils of carbonate and clastic matrix. Guizhou Agric Sci 43, 128–132 (in Chinese).
[56] Xiao, J., Chen, W., Wang, L., Zhang, X.K., Wen, Y.B., Bostick, B.C., et al., 2022. New strategy for exploring the accumulation of heavy metals in soils derived from different parent materials in the karst region of southwestern China. Geoderma 417, 115806.
[57] Yang, Q., Yang, Z.F., Filippelli, G.M., Ji, J.F., Ji, W.B., Liu, X., et al., 2021. Distribution and secondary enrichment of heavy metal elements in karstic soils with high geochemical background in Guangxi, China. Chem Geol 567, 120081.
[58] Ni, S.Q., Ju, Y.W., Hou, Q.L., Wang, S.J., Liu, Q., Wu, Y.D., et al., 2009. Enrichment of heavy metal elements and their adsorption on iron oxides during carbonate rock weathering process. Prog Nat Sci 19 (9), 1133–1139.
[59] Yang, Q., Yang, Z.F., Ji, J.F., Liu, X., Ji, W.B., Wang, J., et al., 2021. Characteristics of mineralogy and heavy metal geochemistry in ferromanganese nodule rich soils with high geochemical background from Guigang, Guangxi. Geoscience 35, 1450–1458.
[60] Wan, D., Zhang, N.C., Chen, W.L., Cai, P., Zheng, L.R., Huang, Q.Y., 2018. Organic matter facilitates the binding of Pb to iron oxides in a subtropical contaminated soil. Environ Sci Pollut Res 25, 32130–32139.